Local Orthorhombic Phase in Zirconium Oxide Nanocrystals: Insights from X-ray Pair Distribution Function Analysis

Rohan Pokratath[1], Kumara Cordero-Edwards[2], Maryame Bina[1], Simon J. L. Billinge[3], and Jonathan De Roo[1,*]

[1]Department of Chemistry, University of Basel, Mattenstrasse 22, 4058 Basel, Switzerland

[2]Catalan Institute of Nanoscience and Nanotechnology (ICN2), CSIC and BIST, Campus UAB, Bellaterra, 08193 Barcelona, Spain

[3]Applied Physics and Applied Mathematics Department, Columbia University, New York, NY, USA

ABSTRACT

Zirconium dioxide (ZrO_2) and hafnium dioxide (HfO_2) have emerged as promising alternatives to conventional ferroelectric materials. Understanding the crystal phases of these oxides under different conditions is crucial for optimizing their properties. While there are several theories for the (anti)ferroelectric properties, comprehensive analysis, particularly at the local structure level, is lacking. In this study, we investigate the local structure of ZrO_2 nanocrystals using X-ray pair distribution function (PDF) analysis, revealing an unexpected local orthorhombic distortion irrespective of crystallite size. This finding suggests the potential existence of an intermediate orthorhombic phase during the microscopic switching pathway observed in previous studies. Additionally, we explore the influence of crystallite size and surface effects on the PDF. These results contribute to a deeper understanding of the structural dynamics in ZrO_2 and offer insights for the design of next-generation ferroelectric materials.

Introduction

Materials that exhibit switchable polarization have garnered significant interest due to their potential application in various fields, e.g., energy storage, energy harvesting, infrared sensors, high permittivity capacitors, Ferroelectric Random Access Memory (FeRAM), Radio Frequency Identification (RFID), and other optoelectronic devices.[1–8] Switchable polarization refers to the ability of certain materials to exhibit a reversible change in the orientation of their electric dipole moment under the application of an external electric field (ferroelectricity), pressure (piezoelectricity), or thermal variations (pyroelectricity).

Since all ferroelectric materials are pyroelectric and piezoelectric, ferroelectricity is a unique behavior, which allows the interchange between electrical, mechanical, and thermal energy. Standard ferroelectric materials, such as $BaTiO_3$, are not compatible with silicon process technologies, leading to a demand for alternative materials. Since 2011, zirconium (ZrO_2) and hafnium oxides (HfO_2) have been considered as a potential replacement.[9]

The crystal phase of both oxides varies with temperature and crystal size.[10] The monoclinic phase is favored under ambient conditions, transitioning to the tetragonal ZrO_2/HfO_2 phase at around 1170/1700 °C and further transforming into the cubic fluorite-type phase at approximately 2370/2600°C. The tetragonal and cubic phases can also be stabilized at room temperature by reducing the crystal size, by cation doping, by oxygen vacancies, by stress/strain, by quenching after crystallization, or by modifying the surface energy.[11,12] For ZrO_2 the tetragonal phase becomes the stable form at room temperature when the crystal size falls below 30 nm, in agreement with the experimental results.[13,14] There have also been reports of 20 nm tetragonal crystals.[15] Conversely, for HfO_2, the tetragonal phase becomes thermodynamically favored when the crystallite size falls below approximately 3.6 nm.[16] This disparity underscores the distinct thermodynamic behavior of these materials.

While both ZrO_2 and HfO_2 exhibit (anti)ferroelectric properties, the crystallographic explanations are often more explicitly provided for the latter.[2,9,17–19] Despite numerous reports on the (anti)ferroelectric properties in ZrO_2[20–24], there is a lack of comprehensive crystallographic analysis, especially of the local structure.[25] The (anti)ferroelectric polarization emerges from a transition from a non-polar to a polar phase. Hoffmann *et. al.* observed the transition between the tetragonal and orthorhombic $Pca2_1$ phase upon the application of an electric field. However, the microscopic switching pathway between the phases remains unclear, with the potential inclusion of an intermediate orthorhombic $Pmn2_1$ phase.[26] In this work, we investigate the local structure of ZrO_2 nanocrystals with sizes ranging from 2.5 - 5.6 nm using X-ray pair distribution function (PDF) analysis. While the structure of these nanocrystals was initially presumed to be tetragonal, our analysis reveals an intriguing local orthorhombic $Pmn2_1$ distortion regardless of crystallite size. This finding untangles the possibility of an intermediate orthorhombic $Pmn2_1$ phase during the microscopic switching pathway observed by Hoffmann *et. al.*. Additionally, we investigate two factors that may influence the short-range PDF: crystallite size and surface effects.

Results and Discussion

Identifying the local distortion

X-ray total scattering with pair distribution function analysis is a well-known technique for the detailed structural analysis of nanostructured and disordered materials.[27] The analysis is particularly useful because it accounts for local distortions in the material, allowing the identification of disorders. ZrO_2 nanocrystals (4 nm in diameter) were synthesized in trioctylphosphine oxide (TOPO) at 340°C, purified, and subsequently analyzed with total scattering.

$$ZrCl_4 + Zr(O\mathit{i}Pr)_4 \cdot \mathit{i}PrOH \xrightarrow[TOPO]{340\ ^\circ C} ZrO_2 + ZrCl_4 + 2\,C_3H_6 + 3\,\mathit{i}PrOH \quad (1)$$

The experimental PDF was modeled with a tetragonal ($P4_2/nmc$) phase, but a significant misfit was observed for the first Zr-Zr peak (3.59 Å). All other peaks showed agreement with the model (Figure 1a). Although the fit is quite good ($Rw = 0.11$), the mismatch observed for the first Zr-Zr peak (3.59 Å) could be attributed to minor variations in the local structure of the synthesized nanocrystals, as compared to the average structure. Conventional powder diffraction techniques are limited in detecting such differences due to peak broadening caused by the small crystallite size.[28] The inset in Figure 1a illustrates the source of the mismatch, indicating that it originates from an experimentally shorter Zr-Zr distance than predicted by the model, while the intensity of the two peaks is similar. A better fit is obtained by dividing the fitting range into two parts, 1.5 - 5 Å (Figure 1b) and 5 - 50 Å (Figure 1c). The refinements were made by fixing the crystallite size to 40 Å. The fit parameters obtained for the 1.5 - 50 Å and 5 - 50 Å ranges show similar values, while those for the 1.5 - 5 Å range are different (Table S1). An increase in the lattice parameter *a*, the isotropic thermal motion parameter (*Uiso*) of oxygen, and a decrease in the lattice parameter *b* are observed in the 1.5 - 5 Å range. The higher *Uiso* values for oxygen in the range 1.5 - 5 Å suggest the presence of local disorder, meaning that the local and average structures differ from each other.

In Figure 1d, short-range X-ray PDF simulations are shown for various ZrO_2 phases, along with their deviation from the observed PDF of the synthesized ZrO_2 nanocrystals. In the cubic phase (Fm-3m) of ZrO_2, only one type of short Zr-Zr spacing is observed at 3.63 Å due to its high symmetry. On the other hand, in the tetragonal phase ($P4_2/nmc$), there are two types of pairs with equal contributions to the peak

intensity, located at 3.59 Å and 3.62 Å. Although the peak positions are very close, a slightly broader peak is observed. Monoclinic ($P2_1/c$) is the most distorted structure among the different ZrO_2 phases, with even shorter Zr-Zr distances ranging from 3.3 to 4 Å. In this case, two broad peaks are observed. Several orthorhombic phases, such as $Pmn2_1$, $Pca2_1$, Pbca, and Pnma, have been reported with average Zr-Zr distances that fall between those of the monoclinic and tetragonal phases.[18] The Zr-Zr spacing observed in the experimental PDF does not match any known polymorphs and falls between the values for the tetragonal and monoclinic phases. The intensity of the second Zr-O peak (between 4 Åand 5 Å) is much lower in the experimental PDF than in the calculated tetragonal phase, and multiple peak contributions are observed in the first Zr-O interaction.

By fitting the local range with various polymorphs, as shown in Figure S1 and Table S2, it was observed that the fits with $P4_2/nmc$ and $Pmn2_1$ were more suitable in terms of peak positions and refined parameters. However, the *Uiso* value of oxygen was higher in the $P4_2/nmc$ model. This suggests that the distortions present in the structure were compensated by using a higher *Uiso* value, leading to a better-fit agreement. Notably, the *Uiso* values obtained for $Pmn2_1$ are relatively lower, and the fit can be substantially improved by allowing additional freedom to the positions of the Zr atoms given that the symmetry is confined (as shown in Figure 1e). The unit cell, before and after refinement of the Zr atom positions, is illustrated in Figure 1f, and the refined parameters are listed in Table S3. However, unlike $Pmn2_1$, no such improvement was observed in the case of $P4_2/nmc$. The findings suggest that the local structure can be described as a slightly distorted $Pmn2_1$ phase, which belongs to the non-centrosymmetric orthorhombic crystal system. The average structure remains assigned to the tetragonal phase though. X-ray diffraction (XRD) patterns of $P2_1/c$, $P4_2/nmc$, and $Pmn2_1$ were simulated for the crystallite size 4 nm (Figure S2). The reflections of $P4_2/nmc$ phase match best with the experimental results.

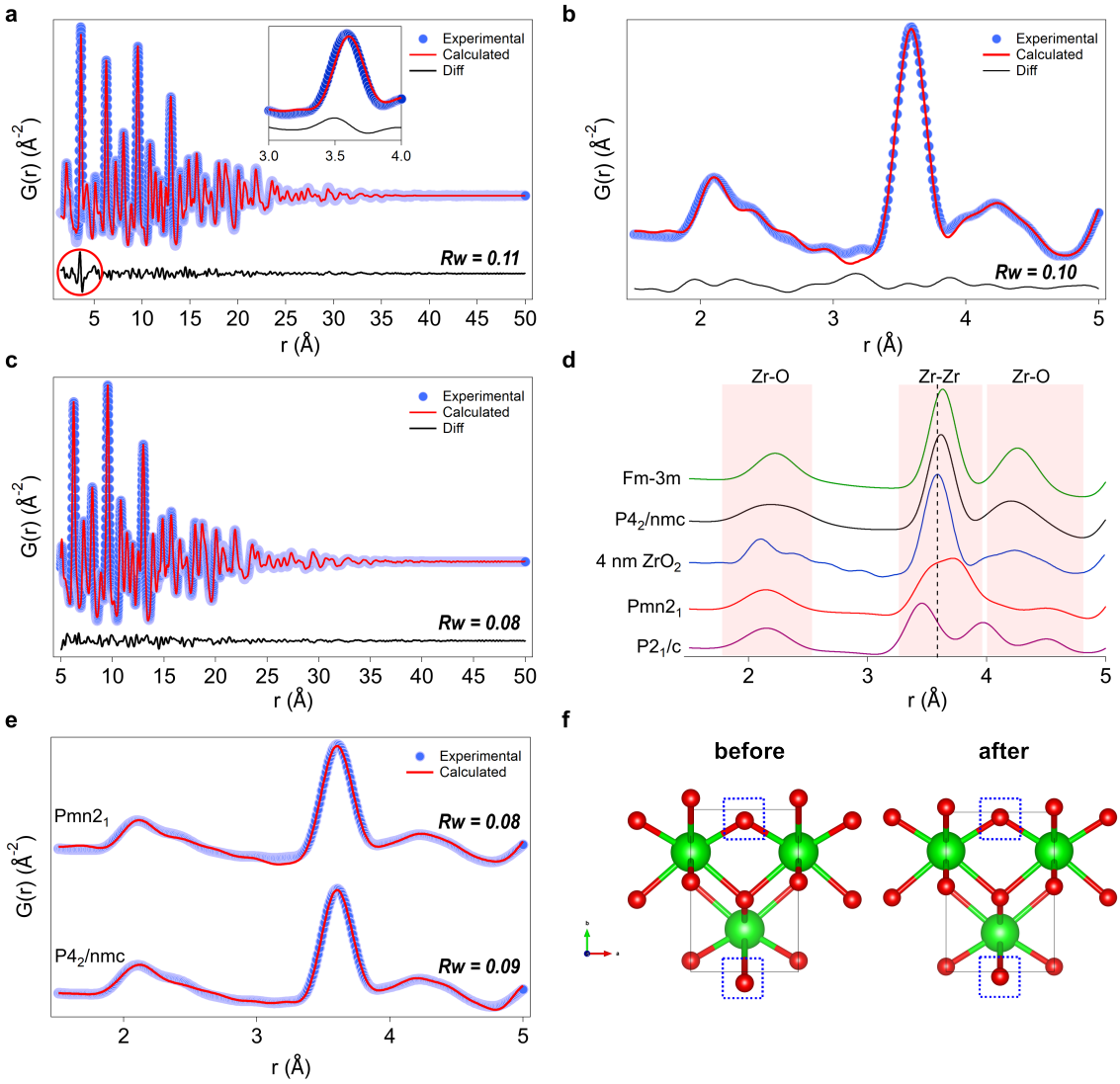

Figure 1 | Experimental and calculated PDF for 4 nm ZrO_2 nanocrystals with tetragonal($P4_2/nmc$) model for the range **(a)** 1.5 - 50 Å, **(b)** 1.5 - 5 Å, and **(c)** 5 - 50 Å. **(d)** Comparison of simulated PDF for different ZrO_2 polymorphs with experimental data. The spacegroup of polymorphs used is indicated. **(e)** Short-range fit obtained for 4 nm ZrO_2 after relaxing the atomic positions of Zr by constraining the symmetry. **(f)** The unit cell of $Pmn2_1$ before and after optimizing the Zr atom position.

Size-dependent structure

ZrO_2 nanocrystals of various sizes are prepared following our previously established size-tuning methods.[29,30] The XRD patterns of the resulting size series can be seen in Figure 2a, and they appear to be similar to the tetragonal phase ($P4_2/nmc$) of ZrO_2. Strong peak broadening is observed for the smaller nanocrystals where the (101) and (002) peaks are overlapping. As the nanocrystal size increases, the peaks become sharper, but no significant changes in the structural features were observed. A distinct difference

is visible in the corresponding signals when transformed to PDF, as shown in Figure 2b. A shift can be observed for the first Zr-Zr peak, which is correlated with the changes in the crystallite size. As the size increases, the peak position increases and shifts towards the position in the pure tetragonal phase (3.61 Å). The shift is more noticeable for smaller nanocrystals. Additionally, it is worth noting that the second Zr-O peak (shaded region in Figure 2b) for the 2.5 nm nanocrystal appears to have split into two, resembling the simulated pattern of the pure monoclinic phase ($P2_1/c$) shown in Figure 1d. The particular pattern between 3.9-5 Å is not a consequence of the small nanocrystal size as shown by the calculated PDFs for different tetragonal crystallites (Figure S3). No reflections of the monoclinic polymorph were detected in the XRD pattern and we thus assign the pattern to a local structural distortion.

Refining the PDFs with the tetragonal phase ($P4_2/nmc$) results in good fits for larger crystals but the fit becomes increasingly poor for crystals smaller than 4 nm, as shown in Figure 2c. For the 2.5 nm nanocrystals, we explored the pure monoclinic phase as an alternative, see Figure S4. The nonphysical refined *Uiso* values rule out the presence of transformation into the monoclinic phase. When the size of the nanocrystals decreases, the proportion of surface atoms compared to those in the core increases. From Figure 2d, it can be seen that the ratio of surface to core atoms (assuming the surface thickness as 4 Å) is approximately 1 when the diameter is 6 nm. As the diameter decreases below 6 nm, the surface atoms dominate over the core atoms. The presence of broken bonds on the terminating surface atoms causes a difference in the bond distance between the surface atom and its nearest neighbor in the core compared to the bulk. The PDFs shown in Figure 2b suggest that the bond length between the Zr atom on the surface and its nearest neighbor may be shorter than average. This could explain the peak shift for very small particles (Figure 2c). Since we do not observe the peak shift in the simulated PDF of nanocrystals (Figure S3) and peak position shifts significantly for smaller crystallite sizes, the observed effect is attributed to the surface defects. Note that even the larger (5nm) particles still feature the particular misfit that we previously attributed to the local orthorombic structure. The surface provides an additional effect on the PDF.

To further investigate the defects at the surface, we performed PDF analysis before and after surface modification. Previously reported findings indicate that the synthesized ZrO_2 nanocrystals are capped with TOPO (trioctylphosphine oxide) and its decomposition products.[31] To eliminate the effect of the ligands from the analysis, we modified the surface by treating it with dilute HCl. Once the ligands exchanged, the

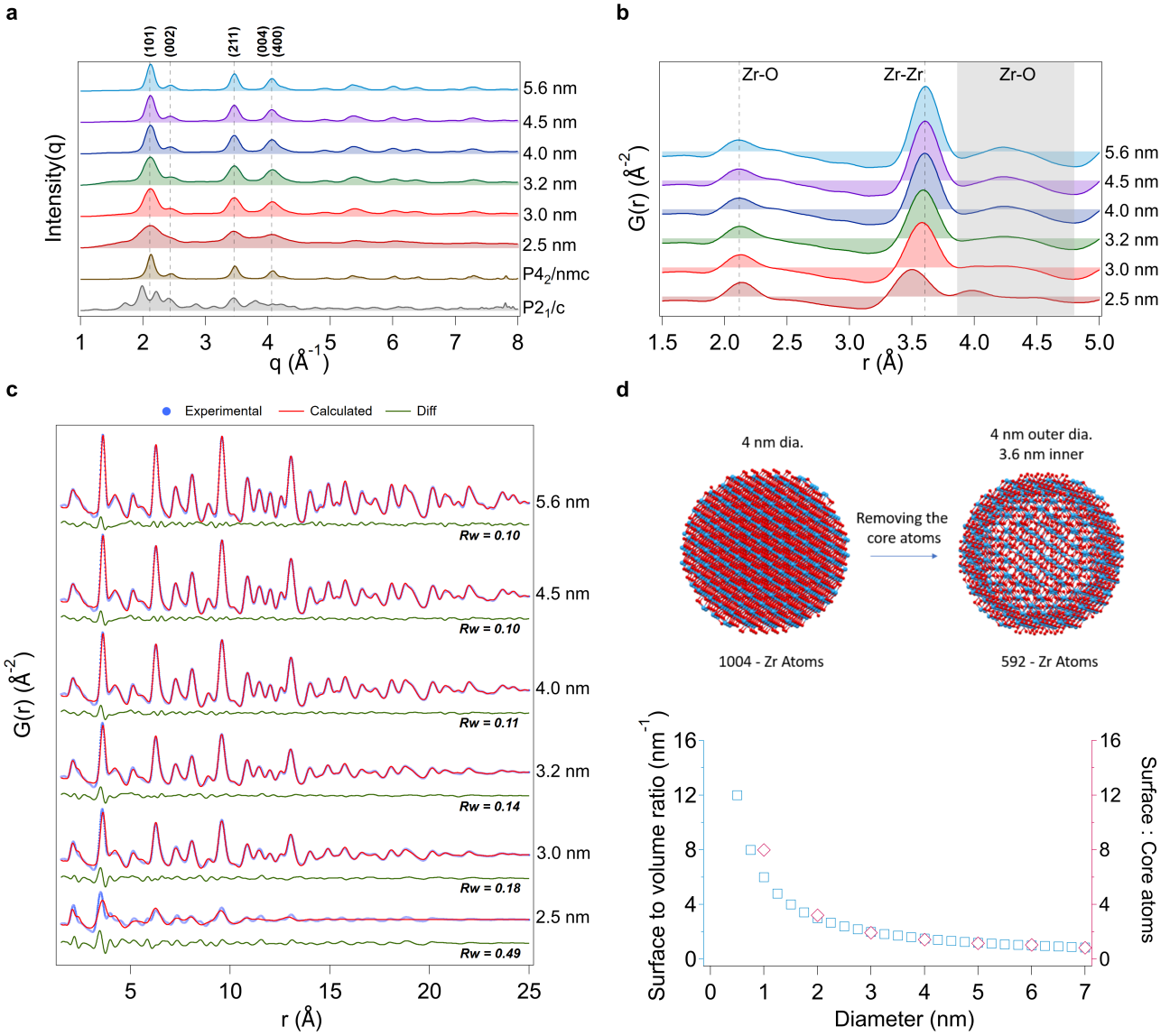

Figure 2 | The **(a)** XRD and **(b)** PDF for ZrO_2 nanocrystal size series. **(c)** Experimental and calculated PDFs for ZrO_2 nanocrystal size series fitted with $P4_2/nmc$. The refined crystallite size (psize) and *Rw* value (goodness of fit) are indicated. Other refined parameters are given in Table S4. **(d)** Surface to volume ratio and surface to core atom ratio for ZrO_2 nanocrystal size series. The intensity of XRD patterns has been normalized for better visualization. The size of the particles was determined from the corresponding PDF refinements and is shown in the figure. In the calculation of the surface atom ratio, a surface thickness of 0.4 nm was assumed, and only Zr atoms were considered for quantification.

surface chemistry altered and the nanocrystals were no longer colloidally stable. We compared the PDF analysis of the surface-modified nanocrystals with the original ones, and no changes were detected in the peak position or refined parameters (Figure S5 and Table S6). This points to the absence of any significant effect of ligands on the PDF.

Efforts to Characterize the Local Dipole

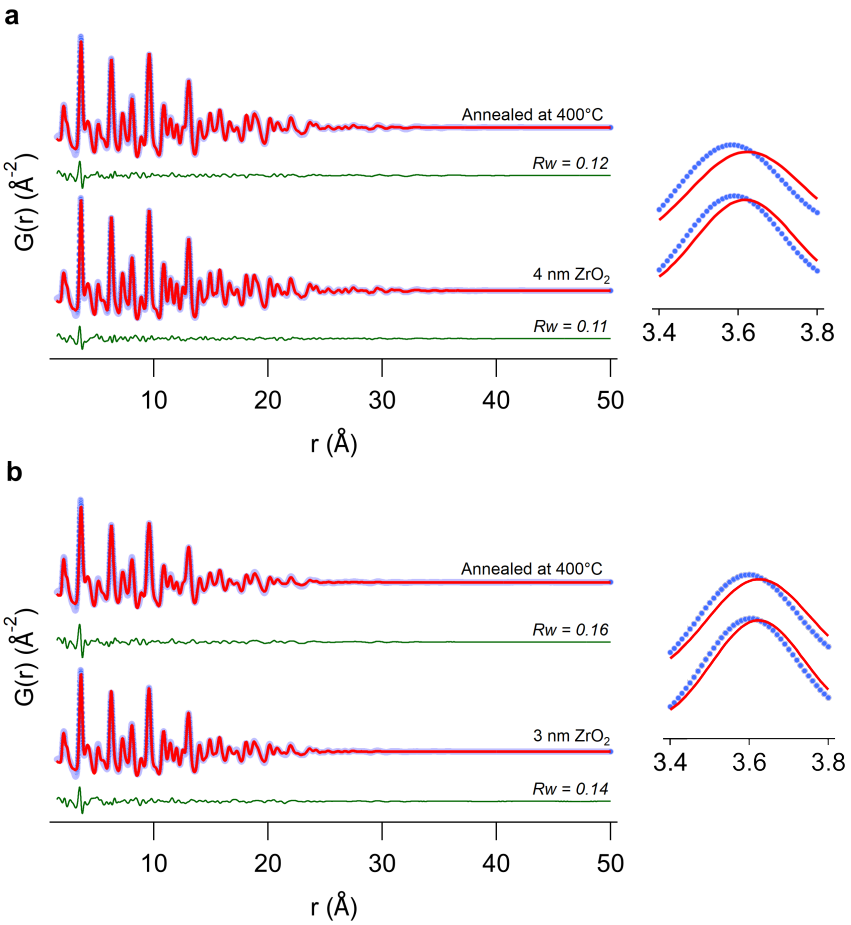

Figure 3 | PDF analysis after heat treatment. The PDF of **a** 4 nm and **b** 3 nm nanocrystals after annealing at 400 °C for 1 hour in air. The misfit at the first Zr-Zr peak is magnified to improve visualization. The refined parameters can be found in Table S6-7.

Since the non-centrosymmetric orthorhombic phase, Pmn21, is ferroelectric, we conducted switching spectroscopy piezoelectric force microscopy (SS-PFM) measurements, which is an effective technique that enables nanoscale mapping of switching parameters by acquiring the local PFM hysteresis loop, to investigate the ferroelectric properties of the ZrO_2 nanocrystals. We prepared ZrO_2 nanocrystal-based thin

films on a conducting electrode via spin coating (see experimental), which were subsequently annealed at 400 °C to enhance the packing efficiency and minimize the ligand fraction. Figure S6 displays the AFM (atomic force microscopy) images obtained before and following annealing. The spin-coat annealing cycle was repeated two times to improve the surface morphology.

We first investigated the effect of the thermal treatment. After annealing the nanocrystals at 400 °C for 1 hour, we observed changes in the PDF of the nanocrystals (Figure 3a-b). The misfit for the first Zr-Zr peak is more pronounced, the crystallite size reduced by about 2 Å, and *Uiso* values of zirconium and oxygen atoms increased (Table S7-8). The higher *Uiso* values indicate more disorder. Based on the fact that there is only a slight reduction in crystallite size and the XRD patterns appear similar (as shown in Figure S7), it can be inferred that the observed effect is confined to the surface and that the overall structure remains the same. While the surface defects could be attributed to phosphate formation upon annealing as shown by Cademartiri *et. al.*,[32] the exact structural changes that occurred at the surface are unclear. The absolute quantification of the contribution of surface defects to the peak shift is also not possible due to the presence of local distortions in the bulk of the crystal.

During SS-PFM measurements a DC voltage (V_{DC}) sweep is applied in combination with a small AC voltage ($V_{AC}\cos(\omega t+\phi)$) to probe the piezo-response.[33] The V_{DC} sweep consists of consecutive on-and-off switching, where the magnitude slowly increases and decreases over multiple cycles approximating a triangle waveform. This produces two types of loops: i) when the V_{DC} is applied, called on-state, and ii) when the V_{DC} is turned off, called off-state. For ferroelectric materials, the choice for a specific state loop depends on the research goals and experimental conditions. When the testing is done on a bare surface without a top electrode (like our case), it's recommended to use the off-state measurements as a way to reduce the electrostatic contribution to the PFM signal.[34] Whereas on-state measurements allow to avoid polarization relaxation between pulses when no DC bias is present.[35] Independently of the state loop measurement, ferroelectrics typically exhibit a butterfly-type amplitude hysteresis loop accompanied by changes in the phase signal. Whilst, in the case of antiferroelectrics, since there is no net polarization in the absence of an external field, the local antiferroelectric behavior is tested in the on-state loop. The results obtained for the thin film with 4 nm and 3 nm nanocrystals are shown in Figure 4. In these measurements the frequency of one cycle was 500 mHz; each cycle started at 0 V and rectangular wave pulses with 90 ms on – 90 ms off were decremented until a final voltage of -8V, upon which the wave pulses were

incremented to 8V, then decremented back up to 0V, giving a full piezoresponse vs. tip bias hysteresis loop. The on-state does not show the typical antiferroelectric loop, and the off-state presents a ferroelectric hysteresis loop, the amplitude signal as a function of bias exhibits the characteristic "butterfly" shape with a finite value at zero bias and two local minima that coincide with a phase shift of almost 180º in the phase signal, which normally corresponds the coercive field. To ensure our findings the measurements were repeated but this time with a frequency of 200 mHz (see Figure S8). In this case, no "butterfly" shape in the amplitude signal and an expected, but distorted, phase shift in the phase signal were observed. This inconsistency in the results could be related to electrostatic effects[36], electrochemical strain[37–39], or any other potential artifacts that are out of the scope of this paper. While SS-PFM can be used to characterize materials already known to be ferroelectric, it is unreliable as actual proof of ferroelectricity. Given also the lack of robustness in our measurements we cannot conclude that the zirconia nanocrystals are ferroelectric. This does not come as a complete surprise since the average structure is the nonpolar tetragonal structure and only the local structure is described by a polar distortion.

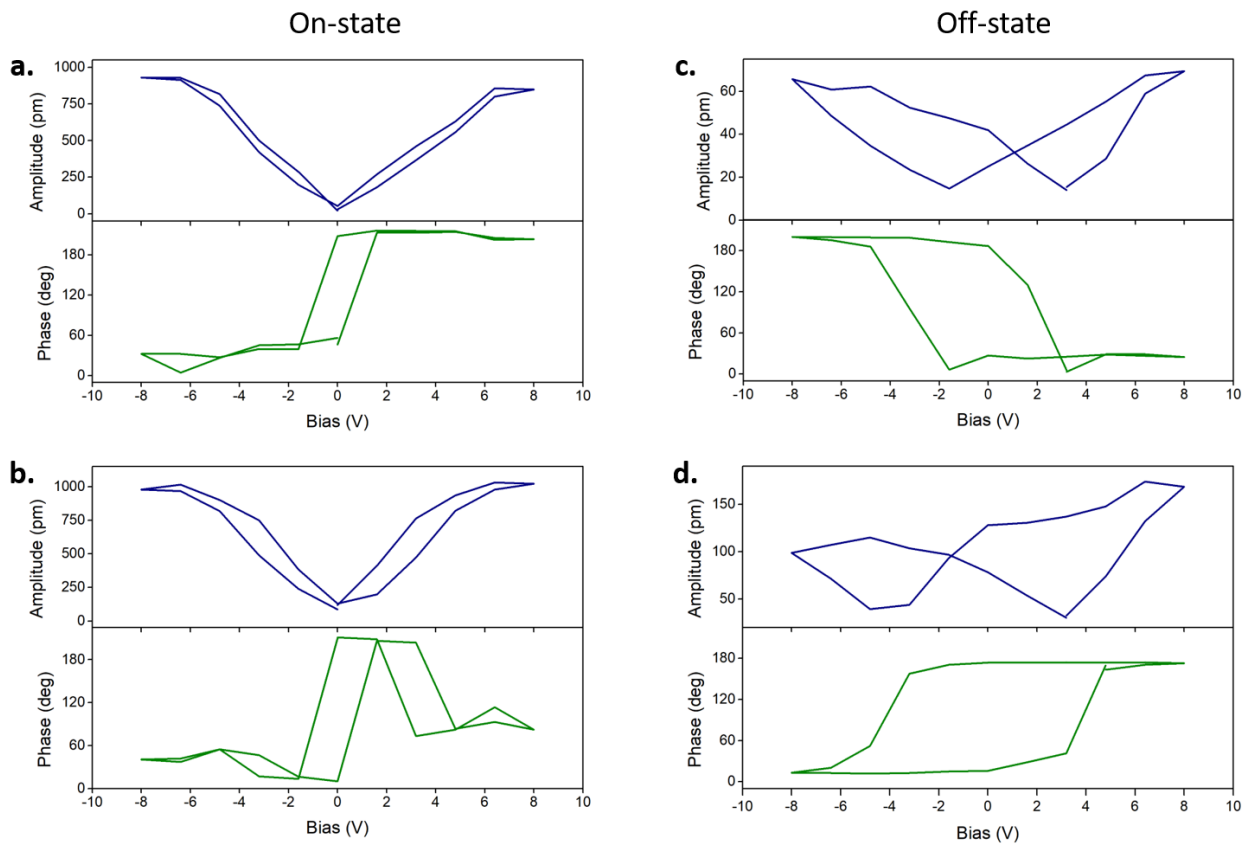

Figure 4 | Hysteresis loop at 500 mHz for ZrO_2 nanocrystals based thin films. a-b On-state and **c-d** off-state hysteresis loop for a 4 nm and 3 nm ZrO_2 nanocrystal thin film.

Conclusion

In conclusion, our investigation using X-ray pair distribution function (PDF) analysis sheds light on the local structure of ZrO_2 nanocrystals, revealing an intriguing orthorhombic distortion irrespective of crystallite size. It suggests the possibility of an intermediate phase contributing to the observed switching pathway, even though we did not find proof of ferroelectricity in layers of annealed nanocrystals.

Experimental

Materials

$ZrCl_4$ (99.9%), $ZrBr_4$ (99%) and $Zr(OtBu)_4$ (99.9%) were purchased from Strem Chemicals and $Zr(OiPr)_4 \cdot iPrOH$ (99.9%), toluene (99.5%), acetone (99.8%) from Sigma Aldrich and used without further purification. Tri-*n*-octylphosphine oxide (99%) was bought from Strem chemicals and recrystal-

lized according to Owen *et al.*[40]

Nanocrytsal synthesis

ZrO_2 nanocrystals are synthesized according to our previously published procedure,[31] which was slightly different from the original procedure of Joo *et al.*[13] Typical amounts were 7.5 g recrystallized TOPO, $Zr(OiPr)_4 \cdot iPrOH$ (0.387 g, 1.5 mmol), and $ZrCl_4$ (0.349 g, 1.5 mmol). To synthesize smaller nanocrystals, either the reaction is stopped based on the temporal evolution of nanocrystal size discussed in the previous chapter or precursor combinations with $ZrBr_4$ or $Zr(OtBu)_4$ are used. Larger ZrO_2 nanocrystals were produced using continuous injection of either $Zr(OiPr)_4 \cdot iPrOH$ or $Zr(OtBu)_4$ into the reaction mixture.[29,30]

Thin film preparation

Purified nanocrystals are dispersed in toluene at a concentration of 100 mg/mL. 50 μL of sample spin-coated on a 12.5 x 12.5 mm indium tin oxide (ITO) coated substrate at 1000 rpm for 30 seconds, followed by moving the substrate to a hot plate at 400 °C. After one hour, the substrate is taken out and allowed to cool to room temperature.

Synchrotron X-ray total scattering experiments

Samples were prepared in 1 mm polyamide kapton tube and were measured at beamline 11-ID-BM at Advanced Photon Source, Argonne National Laboratory, USA. X-ray total scattering data were collected at room temperature in rapid acquisition mode, using a Perkin Elmer digital X-ray flat panel amorphous silicon detector (2048 × 2048 pixels and 200 × 200 μm pixel size) with a sample-to-detector distance of 180 mm (11-ID-BM). The incident wavelength of the X-rays was λ = 0.2110 Å (11-ID-BM). Calibration of the experimental setup was performed using a Ni standard.

Analysis of synchrotron X-ray total scattering data

Raw 2D data were corrected for geometrical effects and polarization, then azimuthally integrated to produce 1D scattering intensities versus the magnitude of the momentum transfer Q (where $Q = 4\pi sin\theta/\lambda$ for elastic scattering) using pyFAI and xpdtools.[41,42] The program xPDFsuite with PDFgetX3 was used to perform the background subtraction, further corrections, and normalization to obtain the reduced total scattering structure function F(Q), and Fourier transformation to obtain the pair distribution function,

G(r).[43,44] For data reduction, the following parameters were used after proper background subtraction: Qmin = 0.8 $Å^{-1}$, Qmax = 22 $Å^{-1}$, Rpoly = 0.9 Å. Modeling and fitting were carried out using Diffpy-CMI.[45]

Surface topology

The morphology of ZrO_2 coatings was investigated using atomic force microscopy (AFM) in air (NanoWizard Ultra, JPK Instruments, Bruker, USA) in intermittent contact mode. Commercially available aluminum reflex coated cantilever Tap150Al-G (nominal resonant frequency 150 kHz, spring constant 5 Nm^{-1}) was used for imaging all the samples in air. Micrographs were collected at a drive frequency of 176 kHz with a line rate of 0.225 Hz. Data was subsequently analyzed with JPK data analysis software.

SS-PFM measurements

SS-PFM was performed using the same setup as PFM as described by Jesse *et al.*.[33] A DC bias (VDC) is applied to the AFM tip in addition to the AC probing voltage (VAC), and the bottom electrode is grounded. The PFM phase and amplitude are then recorded while the DC bias is ramped stepwise, going back to zero bias after each step. This produces two measurements: one as a function of the bias applied at the time of the acquisition ('on'), and one as a function of the bias applied just before the acquisition ('off'). To avoid the effects of electrostatic interactions between tip and sample, only the results of the 'off' state are used. Amplitude and phase signals were recorded using an Asylum Research MFP-3D atomic force microscope (AFM) operating in dual resonance tracking (DART) mode, using Nanosensores PPP-EFM cantilevers with a resonance frequency of 75 kHz and a spring constant of 2.8 N/m.

Acknowledgement

The authors thank the University of Basel and SNF Eccellenza for funding.

Competing interests

The authors declare no competing interests.

Additional information

Supplementary information The online version contains supplementary material available at

References

1. Okuno, J. *et al.* Demonstration of 1T1C FeRAM arrays for nonvolatile memory applications. *2021 20th Int. Work. on Junction Technol. (IWJT)* 1–4, DOI: 10.23919/IWJT52818.2021.9609497 (2021).

2. Boescke, T. S., Mueller, J., Braeuhaus, D., Schroeder, U. & Boettger, U. Ferroelectricity in hafnium oxide thin films. *Appl. Phys. Lett.* **99**, DOI: 10.1063/1.3634052 (2011).

3. Park, M. H., Lee, Y. H., Mikolajick, T., Schroeder, U. & Hwang, C. S. Review and perspective on ferroelectric HfO_2-based thin films for memory applications. *MRS Cummunications* **8**, 795–808, DOI: 10.1557/mrc.2018.175 (2018).

4. Wong, H. S. P. & Salahuddin, S. Memory leads the way to better computing. *Nat. Nanotechnol.* **10**, 191–194, DOI: 10.1038/nnano.2015.29 (2015).

5. Gurfinkel, M., Suehle, J., Bernstein, J. & Shapira, Y. Enhanced gate induced drain leakage current in HfO_2 mosfets due to remote interface trap-assisted tunneling. *2006 Int. Electron Devices Meet.* 1–4, DOI: 10.1109/IEDM.2006.346896 (2006).

6. Lemey, S. *et al.* Wearable flexible lightweight modular RFID tag with integrated energy harvester. *IEEE Transactions on Microw. Theory Tech.* **64**, 2304–2314, DOI: 10.1109/TMTT.2016.2573274 (2016).

7. Wei, X. *et al.* Progress on emerging ferroelectric materials for energy harvesting, storage and conversion. *Adv. Energy Mater.* **12**, 2201199, DOI: 10.1002/aenm.202201199 (2022).

8. Sharma, A. P. *et al.* Lead-free relaxor-ferroelectric thin films for energy harvesting from low-grade waste-heat. *Sci. Reports* **11**, 111, DOI: 10.1038/s41598-020-80480-1 (2021).

9. Böscke, T. S., Müller, J., Bräuhaus, D., Schröder, U. & Böttger, U. Ferroelectricity in hafnium oxide thin films. *Appl. Phys. Lett.* **99**, 102903, DOI: 10.1063/1.3634052 (2011).

10. Van den Eynden, D., Pokratath, R. & De Roo, J. Nonaqueous chemistry of group 4 oxo clusters and colloidal metal oxide nanocrystals. *Chem. Rev.* **122**, 10538–10572 (2022).

11. Garvie, R. C. Stabilization of the tetragonal structure in zirconia microcrystals. *The J. Phys. Chem.* **82**, 218–224, DOI: 10.1021/j100491a016 (1978).

12. Mikolajick, T. & Schroeder, U. Ferroelectricity in bulk hafnia. *Nat. Mater.* **20**, 718–719, DOI: 10.1038/s41563-020-00914-z (2021).

13. Joo, J. *et al.* Multigram scale synthesis and characterization of monodisperse tetragonal zirconia nanocrystals. *J. Am. Chem. Soc.* **125**, 6553–6557 (2003).

14. Depner, S. W., Kort, K. R. & Banerjee, S. Precursor control of crystal structure and stoichiometry in twin metal oxide nanocrystals. *Crystengcomm* **11**, 841–846, DOI: 10.1039/b819948p (2009).

15. Robinson, R. D., Tang, J., Steigerwald, M. L., Brus, L. E. & Herman, I. P. Raman scattering in HfxZr(1−x)O_2 nanoparticles. *Phys. Rev. B* **71**, 218–224, DOI: DOI:10.1103/physrevb.71.115408 (2005).

16. Hunter, O., Scheidecker, R. & Tojo, S. Characterization of metastable tetragonal hafnia. *Ceramurgia Int.* **5**, 137–142, DOI: https://doi.org/10.1016/0390-5519(79)90021-8 (1979).

17. Mikolajick, T. & Schroeder, U. Ferroelectricity in bulk hafnia. *Nat. Mater.* **20**, 718–719, DOI: 10.1038/s41563-020-00914-z (2021).

18. Huan, T. D., Sharma, V., Rossetti, G. A. & Ramprasad, R. Pathways towards ferroelectricity in hafnia. *Phys. Rev. B* **90**, DOI: 10.1103/physrevb.90.064111 (2014).

19. Müller, J. *et al.* Ferroelectricity in simple binary zro2 and hfo2. *Nano Lett.* **12**, 4318–4323, DOI: 10.1021/nl302049k (2012).

20. Lin, B.-T., Lu, Y.-W., Shieh, J. & Chen, M.-J. Induction of ferroelectricity in nanoscale zro2 thin films on pt electrode without post-annealing. *J. Eur. Ceram. Soc.* **37**, 1135–1139, DOI: https://doi.org/10.1016/j.jeurceramsoc.2016.10.028 (2017).

21. Milan, P., Michael, H., Claudia, R., Thomas, M. & Uwe, S. Nonvolatile random access memory and energy storage based on antiferroelectric like hysteresis in zro2. *Adv. Funct. Mater.* **26**, 7486–7494, DOI: https://doi.org/10.1002/adfm.201603182 (2016).

22. Reyes-Lillo, S. E., Garrity, K. F. & Rabe, K. M. Antiferroelectricity in thin-film zro_2 from first principles. *Phys. Rev. B* **90**, 140103, DOI: 10.1103/PhysRevB.90.140103 (2014).

23. Lombardo, S. *et al.* Atomic-scale imaging of polarization switching in an (anti-)ferroelectric memory material: Zirconia (zro2). *2020 IEEE Symp. on VLSI Technol.* 1–2, DOI: 10.1109/VLSITechnology18217.2020.9265091 (2020).

24. Silva, J. P. *et al.* Ferroelectricity and negative piezoelectric coefficient in orthorhombic phase pure zro2 thin films. *Appl. Mater. Today* **30**, 101708, DOI: https://doi.org/10.1016/j.apmt.2022.101708 (2023).

25. Liu, G.-W., Zaheer, W., Carrillo, L. & Banerjee, S. Metastable polar orthorhombic local structure of hydrothermally grown hfo2 nanocrystals. *Cell Reports Phys. Sci.* 101818, DOI: https://doi.org/10.1016/j.xcrp.2024.101818 (2024).

26. Hoffmann, M. *et al.* Antiferroelectric negative capacitance from a structural phase transition in zirconia. *Nat. Commun.* **13**, DOI: https://doi.org/10.1038/s41467-022-28860-1 (2022).

27. Billinge, S. J. L. & Levin, I. The problem with determining atomic structure at the nanoscale. *Science* **316**, 561–565 (2007).

28. Egami, T. & Billinge, S. J. L. Underneath the bragg peaks: Structural analysis of complex materials. *Elsevier* **16**, 2–481 (2012).

29. Pokratath, R. *et al.* Mechanistic insight into the precursor chemistry of zro2 and hfo2 nanocrystals; towards size-tunable syntheses. *JACS Au* **2**, 827–838 (2022).

30. Pokratath, R. *et al.* An amorphous phase precedes crystallization: Unraveling the colloidal synthesis of zirconium oxide nanocrystals. *ACS Nano* DOI: 10.1021/acsnano.3c02149 (2023).

31. De Keukeleere, K. *et al.* Stabilization of colloidal ti, zr, and hf oxide nanocrystals by protonated tri-n-octylphosphine oxide (topo) and its decomposition products. *Chem. Mater.* **29**, 10233–10242 (2017).

32. Shaw, S. *et al.* Selective removal of ligands from colloidal nanocrystal assemblies with non-oxidizing he plasmas. *Chem. Mater.* **30**, 5961–5967, DOI: 10.1021/acs.chemmater.8b02095 (2018).

33. Jesse, S., Baddorf, A. P. & Kalinin, S. V. Switching spectroscopy piezoresponse force microscopy of ferroelectric materials. *Appl. Phys. Lett.* **88**, DOI: 10.1063/1.2172216 (2006).

34. Balke, N. *et al.* Current and surface charge modified hysteresis loops in ferroelectric thin films. *J. Appl. Phys.* **118**, 072013, DOI: 10.1063/1.4927811 (2015). https://pubs.aip.org/aip/jap/article-pdf/doi/10.1063/1.4927811/14740512/072013_1_online.pdf.

35. Alexe, M. & Gruverman, A. *Preface to Nanoscale Characterization of Ferroelectric Materials: Scanning Probe Microscopy Approach* (Springer Berlin, Heidelberg, 2004).

36. Kim, B., Seol, D., Lee, S., Lee, H. N. & Kim, Y. Ferroelectric-like hysteresis loop originated from non-ferroelectric effects. *Appl. Phys. Lett.* **109**, 102901, DOI: 10.1063/1.4962387 (2016). https://pubs.aip.org/aip/apl/article-pdf/doi/10.1063/1.4962387/14483927/102901_1_online.pdf.

37. Jesse, S. *et al.* Electrochemical strain microscopy: Probing ionic and electrochemical phenomena in solids at the nanometer level. *MRS Bull.* **37**, 651–658, DOI: 10.1557/mrs.2012.144 (2012).

38. Adler, S. B. Chemical expansivity of electrochemical ceramics. *J. Am. Ceram. Soc.* **84**, 2117–2119, DOI: https://doi.org/10.1111/j.1151-2916.2001.tb00968.x (2001). https://ceramics.onlinelibrary.wiley.com/doi/pdf/10.1111/j.1151-2916.2001.tb00968.x.

39. Morozovska, A. N., Eliseev, E. A., Balke, N. & Kalinin, S. V. Local probing of ionic diffusion by electrochemical strain microscopy: Spatial resolution and signal formation mechanisms. *J. Appl. Phys.* **108**, 053712, DOI: 10.1063/1.3460637 (2010). https://pubs.aip.org/aip/jap/article-pdf/doi/10.1063/1.3460637/14065633/053712_1_online.pdf.

40. Owen, J. S., Park, J., Trudeau, P. E. & Alivisatos, A. P. Reaction chemistry and ligand exchange at cadmium-selenide nanocrystal surfaces. *J. Am. Chem. Soc.* **130**, 12279–12280 (2008).

41. Ashiotis, G. *et al.* The fast azimuthal integration python library:pyfai. *J. Appl. Crystallogr.* **48**, 510–519, DOI: 10.1107/s1600576715004306 (2015).

42. Wright CJ, Z. X. Computer-assisted area detector masking. *J. Synchrotron Radiat.* **24(Pt 2)**, 506–508, DOI: 10.1107/S1600577517000157 (2017).

43. Juhas, P., Davis, T., Farrow, C. L. & Billinge, S. J. L. Pdfgetx3: a rapid and highly automatable program for processing powder diffraction data into total scattering pair distribution functions. *J. Appl. Crystallogr.* **46**, 560–566, DOI: 10.1107/S0021889813005190 (2013).

44. Yang, X., Juhas, P., Farrow, C. L. & Billinge, S. J. xpdfsuite: an end-to-end software solution for high throughput pair distribution function transformation, visualization and analysis. *arXiv preprint arXiv:1402.3163* (2014).

45. Juhas, P., Farrow, C. L., Yang, X., Knox, K. R. & Billinge, S. J. L. Complex modeling: a strategy and software program for combining multiple information sources to solve ill posed structure and nanostructure inverse problems. *Acta Crystallogr.* 562–568 (2015).